

# **Nonlinear MHD modeling of $n=1$ RMP-induced pedestal transport and mode coupling effects on ELM suppression in KSTAR**

S.K. Kim

*Princeton University\**

S. Pamela

*Culham Science Centre for Fusion Energy*

N.C. Logan

*Lawrence Livermore National Laboratory*

Y.-S. Na and C.Y. Lee

*Department of Nuclear Engineering. Seoul National University*

J.-K. Park, S.M. Yang, and Q. Hu

*Princeton Plasma Physics Laboratory*

M. Becoulet and G. Huijsmans

*Department of plasma physics. CEA*

M. Hoelzl

*Max Planck Institute for Plasma Physics*

Y. In

*Ulsan National Institute of Science Technology*

M.W. Kim, H.H. Lee, J. Lee, and J.H. Lee

*Korea Institute of Fusion Energy*

O. Kwon

*Department of Physics. Daegu University*

E. Kolemen

*Princeton University\* and*

JOREK team

*See the author list of Ref.[47] for a list of current team members*

(Dated: July 18, 2022)

## Abstract

Fully suppressing edge-localized modes (ELMs), e.g., with resonant magnetic perturbations (RMPs), is essential to reach and sustain high-performance steady-state H-mode plasmas because large ELMs can significantly reduce the lifetime of divertor components in future tokamak reactors. RMP-driven ELM suppression in KSTAR has been modeled by coupling the neoclassical transport code PENTRC to the non-linear 3D MHD code JOREK. We have found that the radial transport from the combined effects of the kink-peeling, tearing response, and neoclassical toroidal viscosity (NTV) can explain the pedestal degradation observed in experiments. In addition, it has been found that the RMP response can increase the inter-ELM heat flux on the lower outer divertor by redistributing the heat transport between the divertor plates. In addition to the degraded pedestal, ELM suppression is also attributable to the RMP-induced mode interactions. While the linear stability of peeling-ballooning mode (PBMs) improves owing to the degraded pedestal, the PBM and RMP interaction increases the spectral transfer between edge harmonics, preventing catastrophic growth and the crash of unstable modes. Here, it turns out that the magnetic islands near the pedestal top can play a vital role in mediating the mode interactions.

---

\* Corresponding author: sk42@princeton.edu

## I. INTRODUCTION

The high-confinement mode operation (H-mode)[1] is one of the promising plasma operation scenarios for future fusion devices, such as ITER and DEMO. A typical H-mode plasma has a narrow edge transport barrier (ETB). An edge pedestal forms due to the ETB, and it leads to a significant improvement of global plasma confinement [2]. However, a steep pressure gradient and high edge current density [3] in the pedestal can cause edge localized modes (ELMs) [4]. Large ELMs are generally understood to be triggered by peeling-ballooning modes (PBMs) [5], MHD instabilities driven by the current density (peeling) and pressure gradient (ballooning), respectively. PBMs produce a rapid relaxation of the pedestal profile by convective and stochastic diffusive losses [6], resulting in significant heat loads on the divertor targets. In ITER and DEMO, ELMy heat fluxes on divertor are expected to be on the order of a few  $\text{GW}/\text{m}^2$  [7, 8], which exceeds the engineering limit of the tungsten divertor tiles [9]. Therefore, it is critical to suppress the PBMs for high-performance steady-state operation.

Resonant magnetic perturbations (RMPs) using 3D coils [10] are effective for suppressing ELMs, as has been demonstrated on many tokamak devices [11–18]. The widely accepted model [19] for ELM suppression using RMPs is the reduction of the pedestal confinement and linear stabilization of PBMs due to the transport driven by RMPs. Previous efforts revealed that RMPs cause both collisional and turbulent transport. The former is the result of magnetic island formation, which has been detailed in a number of experimental [20–22] and simulation [23–25] works. For the latter case, experimental observation [26–29] and theories [30–35] have also both shown that edge turbulence occurs in the presence of RMPs. However, both transport mechanisms are having difficulty in fully explaining the experimental results, especially the details of the observed density pump-out although some progress is being made[24, 36–39]. In addition, the linearly stabilized PBMs in this model are inconsistent with the experimental observation where coherent PBM-like mode structures remain after entering the PBM suppression phase [40].

To improve the understanding of the PBM suppression mechanism, a numerical study [39] focused on radial particle transport induced by neoclassical toroidal viscosity (NTV) using a linear approach and found that it can considerably contribute to the pump-out. Nonlinear simulations [41–45] also revealed that PBMs can be suppressed via mode interactions between RMPs and PBMs, and this may explain why filament structures are observed during the suppression phase. However, very few or no approaches consider these effects simultaneously.

In this paper, we report an attempt to consider both NTV and nonlinear PBM physics using the 3D MHD code JOEK[46, 47] coupled to the PENTRC code[48]. Here, PENTRC uses a semi-analytic drift-kinetic formulation to calculate NTV fluxes by plasma response and is integrated with JOEK code to produce RMP-induced response and transports self-consistently. This study confirms that NTV can generate considerable radial particle flux, helping to explain the experimentally observed density pump-out. Interestingly, the pedestal degradation in the experiment is not sufficient alone to suppress PBMs. While the linear stability of PBMs improves owing to the degraded pedestal, the interaction between PBMs and RMPs plays a major role in the non-linear saturation of the PBMs, and thus the suppression of the ELM crashes. The structure of the paper is as follows. Descriptions of the model and experimental observations are given in section 2. Section 3 describes the modeling results on the effect of the plasma response and NTV for pedestal degradation. In sections 4 and 5, modeling results for RMP ELM suppression and the associated nonlinear coupling between the RMP and PBMs are presented. Lastly, the conclusion is drawn in section 6.

## II. SIMULATION SETUP

### A. Numerical model

JOEK is a 3D nonlinear MHD code suitable for diverted tokamaks, which can handle X-point geometries and scrape-off-layer (SOL) regions. The code uses a 5-field reduced MHD model with experimental toroidal rotation and two-fluid effects[45, 49]. In this work, the same ion and electron temperature ( $T = T_i = T_e$ ) and density ( $n = n_i = n_e$ ) are assumed. For the parallel heat diffusivity  $\kappa_{||}$ , Braginskii-like diffusivity is employed. The source and the perpendicular diffusion coefficients for particle and thermal transport are derived by interpretive analysis using transport code ASTRA [50] and measured kinetic profiles. All source and transport coefficients are taken to be constant in time. In this way, the initial plasma profile from the reference time slice can be reproduced and maintained in JOEK before applying RMPs. This approach can mimic the anomalous turbulent transport in the core and pedestal region but cannot capture its variation in time, which is a limitation of the heuristic transport model used here.

JOEK is used to calculate the fully 3D and nonlinear plasma response to applied RMPs. NTV theory, which has been developed within a linear perturbative framework, calculates the transport

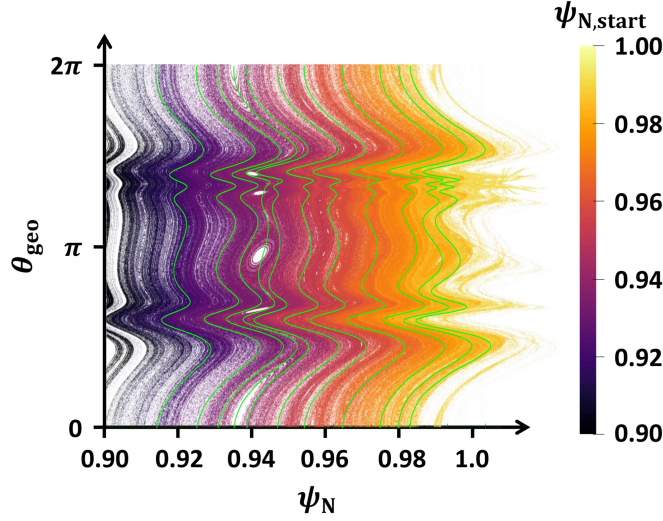


FIG. 1. Perturbed plasma and field lines vs  $\psi_N$  and poloidal angle  $\theta_{\text{geo}}$ . The Poincare plot shows the perturbed field lines, colored to show their respective starting  $\psi_N$  value,  $\psi_{N,\text{start}}$ , while the solid blue contour lines show the perturbed plasma field from Eq. (1).

across perturbed flux surface. To define this perturbed displacement ( $\vec{\xi}$ ) of flux surfaces in JOREK, we define its radial component as Eq. (1) with the temperature in equilibrium,  $T_0$ , and temperature perturbation[51],  $\delta T$ , assuming the uniformity of temperature along the field lines resulting from the strong parallel heat transport in the JOREK simulation.

$$\xi_\psi = \delta T / \nabla_\psi T_0 \quad (1)$$

Figure 1 shows the example of comparison between the plasma displacements obtained directly from the field line tracing and the one using Eq. (1) and data obtained the reference case shown in Fig.1. Here,  $\psi_N$  is the normalized poloidal flux, and  $\theta_{\text{geo}}$  is defined as

$$\theta_{\text{geo}} = \arctan \left[ \frac{Z - Z_0}{R - R_0} \right], \quad (2)$$

where  $(R_0, Z_0)$  is the location of the magnetic axis in the  $(R, Z)$  coordinate. The perturbed temperature (blue lines) displacement approximation captures the kink displacements well throughout the majority of the plasma volume, and smooths over the small island structures revealed by the field line tracing. The approach in Ref. [45, 52] is used to model the RMP application, and plasma response. In the resulting 3D equilibrium, the action of a charged particle is not conserved on a single flux surface, and particles drift radially across flux surfaces at rates determined by their

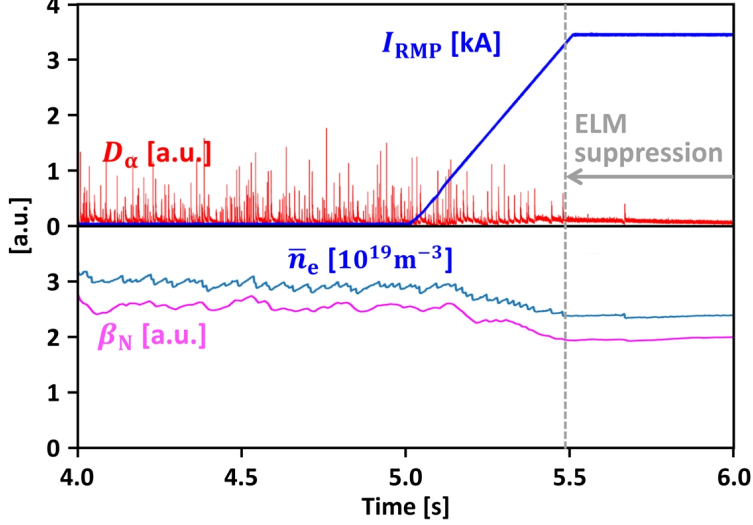


FIG. 2. Experimental time evolution of KSTAR discharge #21072, showing a) RMP coil current  $I_{\text{RMP}}$  (blue line), together with the  $D_\alpha$  signal (red line); and b) the line averaged density  $\bar{n}_e$  (blue line), together with the normalized global beta  $\beta_N$  (red line).

charge and mass[53]. The associated non-ambipolar, neoclassical particle fluxes,  $\Gamma_{\text{NTV}}$ , are calculated from the PENTRC code[48]. This code utilizes a semi-analytic drift-kinetic formulation that is valid across all collisionality regimes to calculate the neoclassical transport for a given non-axisymmetric displacement[54] and calculates this numerically to include all the geometric coupling terms[48].

## B. Plasma configuration

The KSTAR discharge #21072 is used in this simulation, where ELMs are suppressed by  $n=1$  RMPs. An overview of the discharge is shown in Fig. 2; with major radius ( $R_0=1.8$  m), toroidal field ( $B_{\phi 0}=1.8\text{T}$ ), plasma current ( $I_p=0.54$  MA), edge safety factor ( $q_{95} \sim 5.2$ ), global poloidal beta ( $\beta_p \sim 1.9$ ), and line average density ( $\bar{n}_e \sim 3 \times 10^{19} \text{m}^{-3}$ ). In this discharge, an  $n=1$  dominated resonant magnetic perturbation is applied[14] with  $90^\circ$  phasing between rows. Small sideband modes of  $n > 1$  are present in the experiment due to the geometry of the RMP coils, but they are ignored in this study. When the stationary state is reached in the experiment ( $\sim 5.0$  s), the RMP coil current,  $I_{\text{RMP}}$ , gradually increases with the rate of  $\sim 6.8$  kA/s up to 3.45 kA and then rotates toroidally. The ELM suppression begins at 5.5 s with  $I_{\text{RMP}} \sim 3.4$  kA. This simulation uses  $t=4.95$  s (before RMP application) as a reference time.

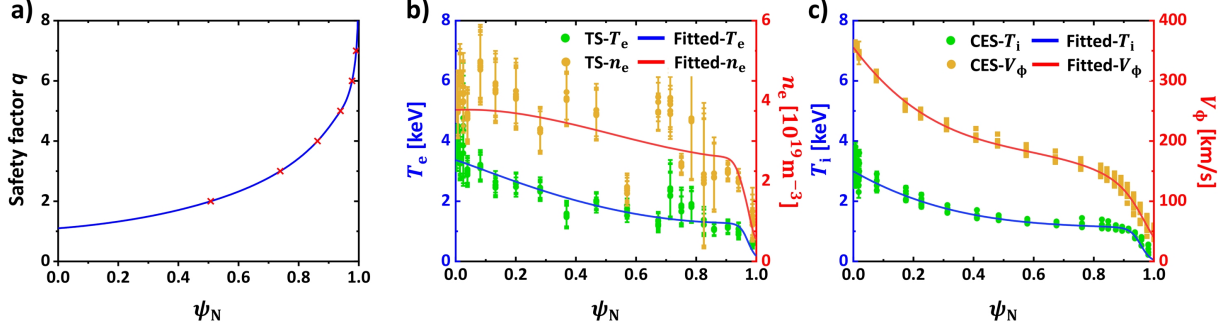


FIG. 3. a) Radial profile of safety factor  $q$  (blue line) and radial location of  $n=1$  rational surfaces (red dot). b) Fitted radial profiles of electron temperature (blue line),  $T_e$ , and density (red line),  $n_e$ , with the measured data from Thomson scattering diagnostics and pedestal adjustment. c) Fitted radial profiles of carbon C6+ ion temperature (blue line),  $T_i$ , and toroidal rotation (red line),  $V_\phi$ , with the measured data from charge exchange spectroscopy diagnostics.

The simulation uses a kinetic equilibria from the EFIT code [56] as an initial condition. Charge exchange spectroscopy (CES) [57] and Thomson scattering (TS) [58] diagnostic data are used to reconstruct the temperature and density profiles. The resulting  $q$  and kinetic profiles are shown in Fig. 3. Here, the measured electron density and temperature pedestals have uncertainty due to the limited spatial resolution and error bars. These pedestal profiles are adjusted within the experimental uncertainty to improve the consistency between measured and simulated PBM properties. The approach in Ref.[45, 59] is used to make the equilibrium linearly unstable to PBM and to match the mode properties of 2D-Electron Cyclotron Emission Imaging spectroscopy (ECEI)[60, 61]. Here, the same scale factors of pedestal height and width are applied to the initially fit  $n_e$  and  $T_e$  pedestals using measured data and hyperbolic-tangent function to match above constraints. The result is shown in Fig. 4. The yellow star represents the initially fit pedestal profile, the pink line is the marginal PBM stability limit from the MISHKA1 code [62], and the gray line corresponds to the pedestal profile whose dominant PBM mode has  $n=6$  consistent with the measurements from ECEI ( $6 \pm 1$ ). As shown in the figure, these two constraints are satisfied by increasing the initial electron density and temperature pedestal heights by 10% (blue star). Therefore, the final equilibrium has higher electron pedestals than the original reconstruction. Additionally, because of difference in measured ion ( $T_{i,\text{exp}}$ ) and electron ( $T_{e,\text{exp}}$ ) temperatures, initial temperature and total pressure in the simulation is set to  $(T_{i,\text{exp}} + T_{e,\text{exp}})/2$  and  $n_e(T_{i,\text{exp}} + T_{e,\text{exp}})$ , respectively.

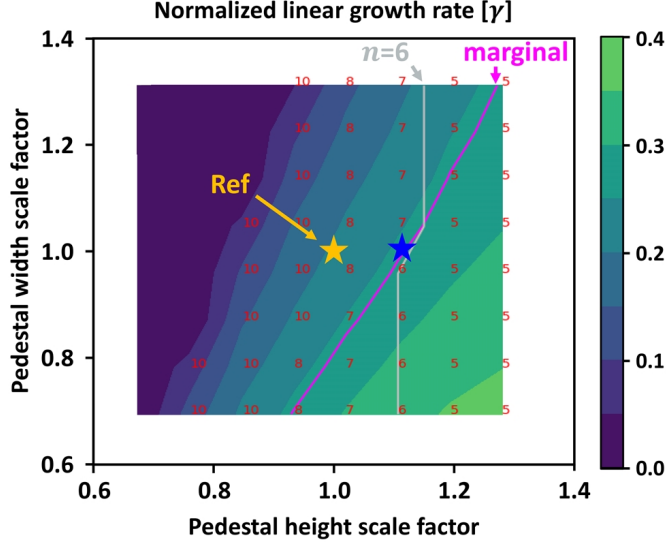


FIG. 4. Normalized linear growth rate of the most unstable PBM vs pedestal height and width scale factors. The mode number  $n$  of the most unstable mode is shown. The magenta and gray lines are the marginal stability limit and the  $n=6$  contour, respectively. The yellow and blue stars represent the initially fitted point and newly adjusted pedestal from the simulation, respectively. Here, the growth rate is normalized by ion-diamagnetic frequency [55]

### C. Modeling Assumptions, Limitations and Initial Simulations Without RMPs

In the simulation, a Braginskii-like viscosity is used with the core value of perpendicular ( $\nu_{\perp}=5.7 \times 10^{-7} \text{m}^2 \text{s}^{-1}$ ) and parallel ( $\nu_{\parallel}=5.7 \times 10^{-6} \text{m}^2 \text{s}^{-1}$ ) components. To avoid the numerical problems, a resistivity 30 times larger than the neoclassical value ( $2.5 \times 10^{-8} \Omega \text{m}$  at  $\psi_{\text{N}} = 0$ ) is applied, which is the important limitation of this work. In particular, recent numerical studies [24, 63, 64] revealed that the RMP field penetration threshold could not be captured with the amplified resistivity because the plasma shielding effect weakens. Therefore, we focus on where the field is fully penetrated, and ELMs are suppressed rather than the RMP penetration processes itself. Here, modeled resistivity has a Spitzer-like temperature dependence. We note that the modeling shown in this work does not consider the slow evolution of the background source and diffusion profiles and describes the RMP-induced short-time evolution from the initial conditions. In future work, these effects will be needed to be included for more realistic simulation.

Before moving to the RMP modeling, the natural PBM stability without the RMP application is checked with the JOEK code. First, single harmonic runs with  $n=1-8$  are launched to model

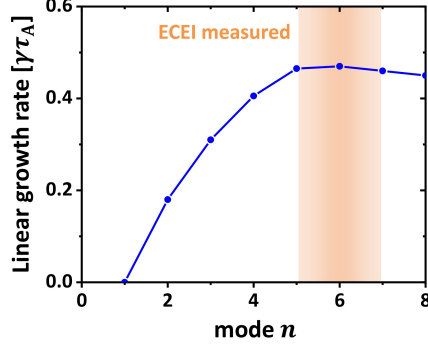


FIG. 5. Normalized linear growth rate spectrum of PBM vs mode  $n$  calculated from the JOREK simulation. The range consistent with the toroidal mode number  $n$  from ECEI diagnostics is colored as an orange area.

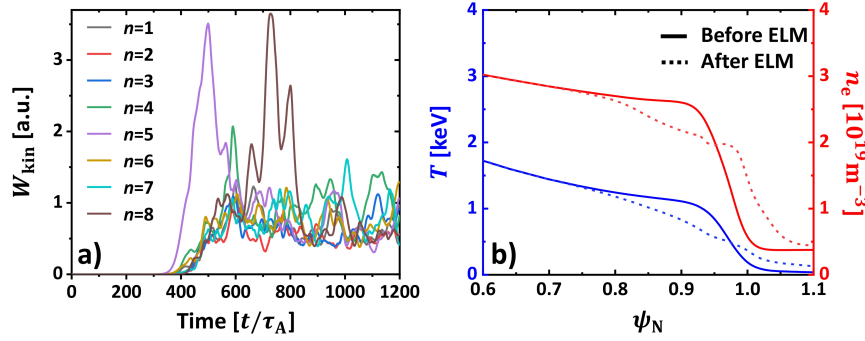


FIG. 6. a) Time evolution of the PBM harmonics of the kinetic energy for  $n=1-8$ . b) Comparison of  $T$  and  $n_e$  before the onset of PBMs ( $\sim 300\tau_A$ ) and after the crash ( $\sim 1200\tau_A$ ).

the linear properties of PBMs. Figure. 5 shows the calculated linear growth rate whose maximum value is  $\gamma\tau_A \sim 0.054$  with  $n=6$ , and  $\tau_A$  is the Alfvén time ( $\sim 0.4\mu\text{s}$ ). In addition, the  $n=6$  mode shows poloidal rotation in the ion-diamagnetic direction with  $V_{\theta,\text{mode}} \sim 6.2$  km/s, showing a good consistency with the measured value ( $\sim 6.85$  km/s) from the ECEI measurement.

A nonlinear PBM calculation is conducted as a next step, including multiple harmonics. Here, the harmonics of  $n > 8$  have been excluded to meet the limits of the computational resources, which is one of the limitations of the simulation. Figure. 6(a) shows the nonlinear evolution of perturbed kinetic energy  $W_{\text{kin}}$  of the PBMs.  $n=5$  are the fastest growing modes, entering the nonlinear phase first. Then, nonlinear mode interactions [49, 65, 66], lead to the large mode crashes [49, 67]. Figure 6(b) shows the simulated profile change at  $\sim 1200\tau_A$ . The density and temperature profiles collapse due to the PBM crash, showing a 26% and 21% decrease of pedestal height, respectively. The stored energy is also reduced by  $\Delta W_{\text{ELM,im}} \approx 7.8$  kJ, which is similar to the measured value

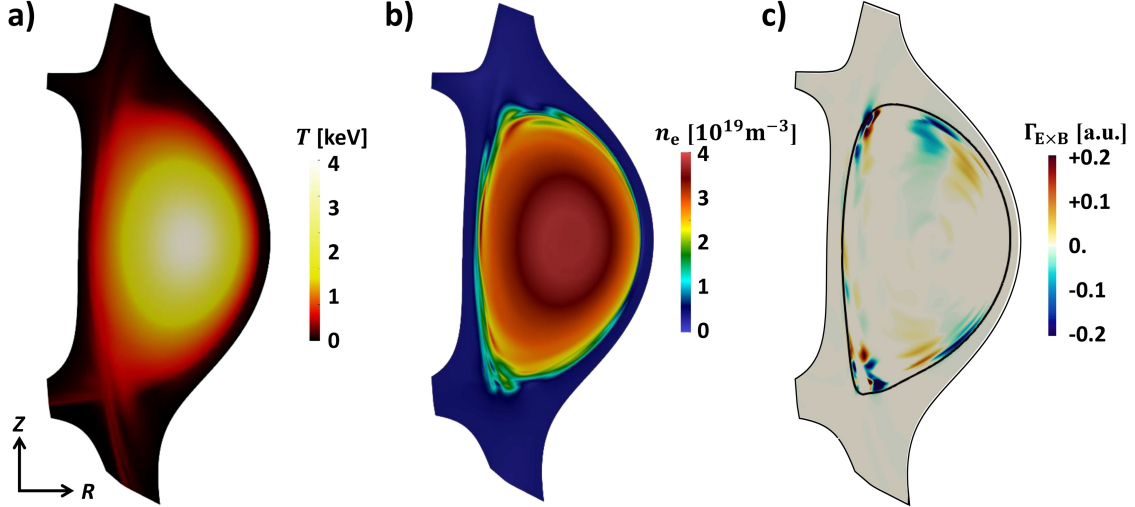


FIG. 7. 2D distribution of a)  $T$ , b)  $n_e$ , and c)  $n=0$   $E \times B$  radial particle flux,  $\Gamma_{E \times B}$ , induced by 3.5kA RMPs in JOREK. The black contour line in c) shows the separatrix boundary.

$\Delta W_{\text{ELM,Exp}} \approx 8(\pm 3.8)\text{kJ}$  from the diamagnetic loop [68].

### III. PLASMA RESPONSE TO RMPS

#### A. KPM and tearing response

An approach similar to the one used in Ref. [52] is employed in this simulation to model the RMPs. We apply the vacuum RMP field [69] to JOREK computational boundary ( $\psi_N = 1.25$ ) as a modified boundary condition, and consider the plasma response after  $\sim 1000\tau_A$  as a RMP-driven equilibrium response. Here, only  $n=0$  (mean) and  $n=1$  (RMP) harmonics are included in the modeling to focus on pure RMP-driven response. We note that the  $n=1$  mode is linearly stable without RMPs and therefore,  $n=1$  is an externally driven response. In the following simulations, RMPs of  $I_{\text{RMP}}=3.5$  kA are included for which ELM suppression is achieved. In the simulation, the Braginskii-like viscosity is used with the core value of perpendicular ( $\nu_{\perp}=5.7 \times 10^{-7}\text{m}^2\text{s}^{-1}$ ) and parallel ( $\nu_{\parallel}=5.7 \times 10^{-6}\text{m}^2\text{s}^{-1}$ ) components. To avoid the numerical problems, 30 times larger resistivity than the neoclassical value ( $2.5 \times 10^{-8}\Omega\text{m}$  at  $\psi_N = 0$ ) is applied, whiing the experiment. The perturbed temperature and density by RMPs are presented in Fig. 7(a) and (b), respectively. As shown in the figure,  $n=1$  perturbations occur in the edge region, showing kink-peeling mode (KPM) characteristics, which is consistent with the previous studies[23, 51, 70]. In addition,

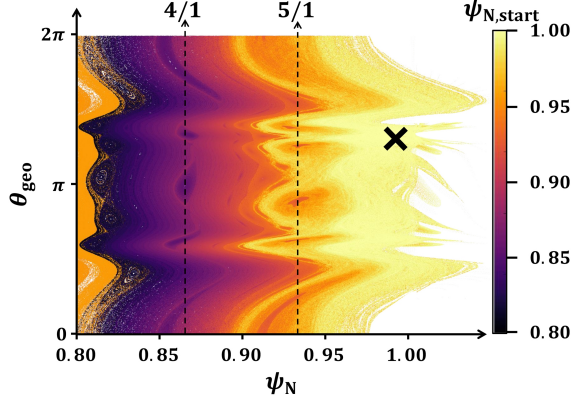


FIG. 8. Poincaré plot of perturbed field structure vs  $\psi_N$  and  $\theta_{\text{geo}}$ . The stochastic layer is formed at  $\psi_N > 0.94$ . The radial locations of  $n=1$  rational surfaces and X-point are represented by the dotted lines and black cross, respectively.

KPM-induced radial  $E \times B$  flow is also observed,  $\Gamma_{E \times B}$ . Figure. 7(c) presents the distribution of  $\Gamma_{E \times B}$ , showing its radial distribution at  $\psi_N = 0.96 - 1.0$ . This can result in  $n=0$  radial convective fluxes and pedestal degradation [45].

Although plasma shielding responses reduce the island sizes relative to vacuum island widths [37], a considerable field penetration is observed in the pedestal region for these simulations with 3.5kA RMPs. The islands form in the pedestal region overlap, and create a stochastic layer. This can be observed in the Poincaré plot in Fig. 8. The figure shows a large island at the resonant surface ( $q = 5/1$ ) near the pedestal top and a stochastic layer at  $0.94 \leq \psi_N \leq 1.0$ . We note that such a large island is due to a weakening of RMP shielding by the larger resistivity used in the simulation. However, previous studies [63] reported that large islands still occur in ELM suppression when a realistic resistivity is used, as a sufficient RMP strength must overcome the shielding effects[71] and to obtain the pedestal top island necessary for suppression. Therefore, although the underlying reasons are different, it can be seen that the size of the fully penetrated magnetic island obtained from this simulation is reasonable. However, it is still questionable whether islands by nonlinear penetration processes and large resistivity will share the same characteristics. This reminds us of the limitations of this modeling and emphasizes the need for future work using realistic resistivity.

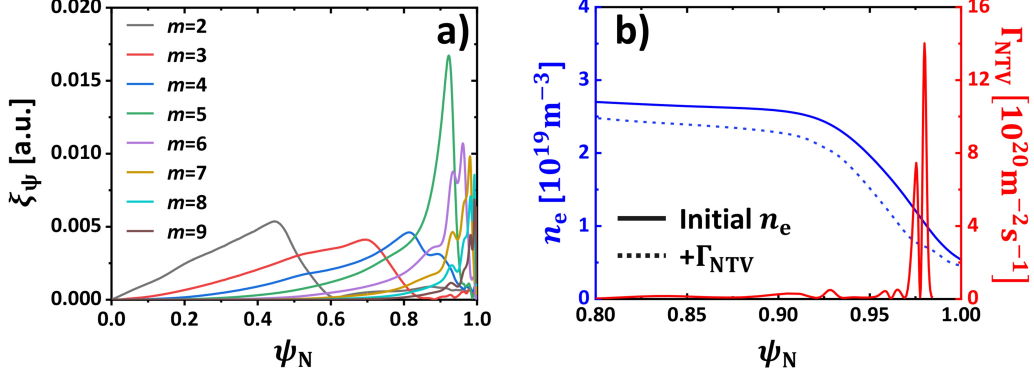


FIG. 9. a) Radial structure of the plasma displacement,  $\xi_\psi$ , induced as an RMP response, showing an edge localized structure. b) The calculated NTV particle flux,  $\Gamma_{\text{NTV}}$ , and the comparison of  $n_e$  profiles without and with  $\Gamma_{\text{NTV}}$  effect.

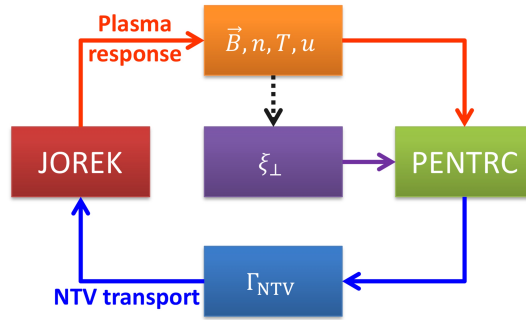


FIG. 10. Schematic diagram of code coupling between JOREK and PENTRC codes.

## B. NTV and mean pedestal degradation

The RMP-induced KPM and magnetic islands generate convection cells and a stochastic layer, which can lead to increased radial transport in the pedestal region. In addition, the plasma displacement by these responses drives neoclassical toroidal viscosity (NTV) [72]. To investigate this effect, ion-NTV transport is included in the JOREK code. An NTV calculation using the PENTRC code requires the axisymmetric magnetic fields, the kinetic profiles, and RMP induced displacements  $\xi_\psi$ , all of which can be obtained from JOREK. For example, Fig. 9(a) shows  $\xi_\psi$ , which comes from the plasma responses in Fig. 7(a) and Eq. (1). Using this information, JOREK and PENTRC are combined. A schematic diagram for the code coupling is presented in Fig. 10. By transferring the response profiles from JOREK to PENTRC, the NTV particle flux  $\vec{\Gamma}_{\text{NTV}}$  and torque  $\tau_{\text{NTV}}$  are calculated. After that, the NTV flux is included in the ion-particle equation as

$S_\rho = -\nabla \cdot \vec{\Gamma}_{\text{NTV}}$ . This process is repeated until the equilibrium converges. Figure 9(b) shows the simulated  $\Gamma_{\text{NTV}}$  with an edge localized structure similar to the  $\xi_\psi$  profile. Here,  $\Gamma_{\text{NTV}}$  results in local profile flattening and considerably reduces the mean ( $n=0$ )  $n_e$  pedestal. For example, as presented in Fig. 9(b),  $\Gamma_{\text{NTV}}$  degrades the  $n_e$  pedestal height by 10% of the initial value. This degradation is 40% of the experimental value, suggesting that NTV can be an important physics mechanism for the density pump-out by RMPs. We note that NTV also induces a thermal heat flux, that is ignored in this work as its amplitude is small in the considered case. This is in line with the experimental trend where the degradation of the density pedestal is much larger than that of the temperature pedestal.

Nevertheless, there is a limit to the presented NTV calculation in that the derived NTV torque at the pedestal is unlikely to be consistent with the experimental value. In the simulation,  $\tau_{\text{NTV}} \sim 6.1 \text{ N} \cdot \text{m}$  while input torque from neutral beam injection (NB) is  $\tau_{\text{NBI}} \sim 3.7 \text{ N} \cdot \text{m}$ . This implies that the calculated  $\Gamma_{\text{NTV}}$  must be overestimated. One possible reason for such a large  $\tau_{\text{NTV}}$  may be due to the approximation of  $\xi_\psi$ . Equation 1 assumes a uniform plasma temperature along field lines. However, this becomes invalid with strong stochastic field lines, which are present in our case. The derived NTV fluxes seem to be overestimated in this stochastic limit. Additionally, the resistivity can affect the NTV by changing the field topology and stability of the peeling response, and the large resistivity used in this study may contribute to overestimated NTV for these reasons. The sensitivity and validity of the NTV modeling have to be investigated in future work for RMP-induced particle transport. Note that NTV is not included in the current plasma momentum modeling. As the NTV induces net torque of the beam drive torque level, it might be expected to alter the plasma rotation away from experimental levels significantly. Because the plasma flow also affects the NTV [39], however, it is possible that the change of rotation would, in turn, reduce the  $\Gamma_{\text{NTV}}$  calculation. Therefore,  $\tau_{\text{NTV}}$  could also be included in future studies for more self-consistent simulations.

Increased radial transport due to the plasma response (tearing and KPM) to RMPs also degrades the mean ( $n=0$ ) pedestal gradient. Figure 11 shows the mean pedestal profiles of  $n_e$  and  $T$ , which are degraded by plasma response and NTV. The further degradation of the  $n_e$  and  $T$  pedestals from the NTV-only case appears because of the increased radial transport by tearing and KPM components. These simulation results show 33% and 30% degradation of the initial  $n_e$  and  $T$  pedestals, respectively. This suggests that the pedestal degradation by RMPs is attributable to both fluid (plasma response) and kinetic effects (NTV). Previous experimental findings show that the

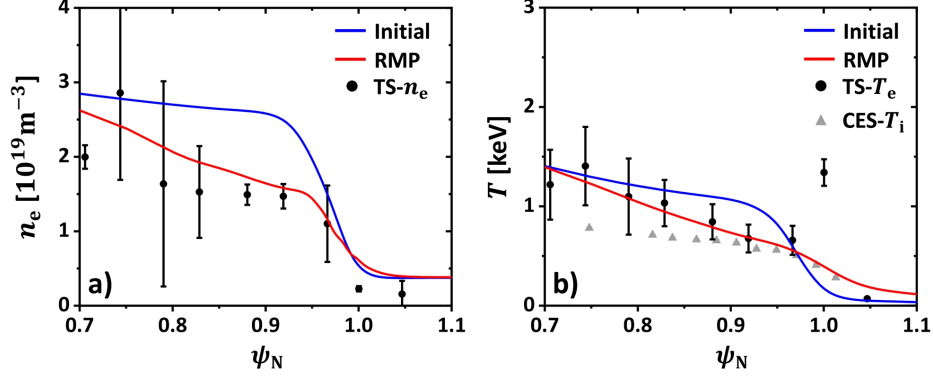


FIG. 11.  $n=0$  profile degradation of a)  $n_e$  and b)  $T$  pedestals due to RMP application in simulations including NTV. It shows the profile comparison before (blue line) and after RMP (red line). The measured profiles from TS and CES diagnostics when RMP is fully established are drawn as the scattered points.

density pump-out under RMPs is highly correlated with X-point deformation [70, 73]. As KPMs cause a large displacement at the X-point, it may play an important role in the density pump-out by forming  $\Gamma_{\text{ExB}}$  and inducing  $\Gamma_{\text{NTV}}$ , which exhibits similar trends to experimental observation.

The above modeling can quantitatively capture the degradation of the  $n_e$  and  $T$  pedestals by RMPs in this KSTAR discharge. However, the degradation of the temperature pedestals is not fully explained in this simulation. The  $T$  pedestal in the simulation matches the experimental  $T_e$  pedestal well but shows considerable deviation from the  $T_i$  pedestal. In addition, the pump-out in the modeling might be interpreted as incomplete insofar as the  $\Gamma_{\text{NTV}}$  may have been overestimated in the modeling, while the resulted  $n_e$  pedestal shows a good agreement with an experimental profile in Fig. 11.

The discrepancy between the experimental and the simulation results could be a consequence of limitations in the simulation model. This study uses a single temperature ( $T = T_i = T_e$ ) and a heuristic perpendicular transport model. Since thermal decoupling, diffusion coefficients, and background conditions (neutral pressure build-up, wall loading, wall temperature) affect the pedestal profiles, this assumption can miss important physics. Previous studies also revealed that the destabilized ballooning modes [44], magnetic flutter [74, 75], polarization effect [24, 76], and RMP-induced micro-instabilities [34, 77] could increase the pedestal transport. Future computational developments, including these additional physics features, will be needed to complete the physics understanding.

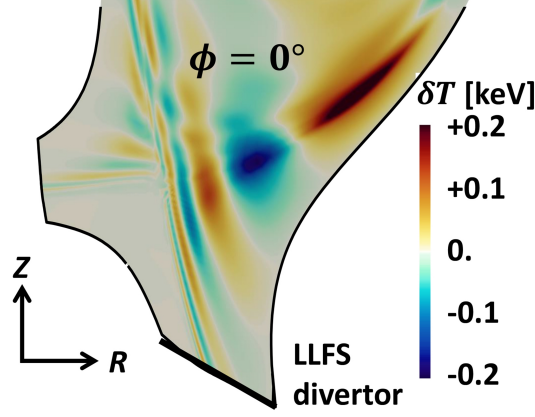


FIG. 12. 2D distribution of the  $T$  perturbation at  $\phi = 0^\circ$ . The divertor at the lower-LFS is marked by a solid black line.

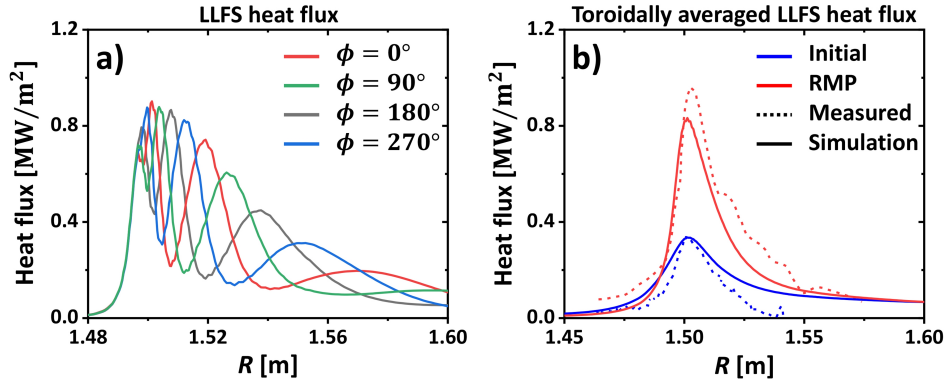


FIG. 13. a) Calculated radial heat flux profiles on LLFS divertor for different toroidal angles  $\phi = 0 - 270^\circ$ . b) Comparison of toroidally averaged heat flux profiles before (blue) and after RMP application (red). The solid and dotted lines present the simulated and measured values, respectively.

### C. Divertor heat flux

The divertor heat flux during the inter-ELM phase with RMPs is also investigated. The KPM response to RMPs induces strong homoclinic tangles. These tangles allow for parallel heat flux into the SOL and lead to 3D temperature profiles near the divertor region, affecting the divertor heat flux. Figure 12 presents such a perturbed temperature distribution in the simulation at  $\phi = 0^\circ$ , where  $\phi$  denotes the toroidal angle. The tangles feature toroidally asymmetric structures resulting in a non-axis-symmetric heat flux distribution. Figure 13(b) presents the modeled heat flux on the lower divertor plate at the low-field side (LFS) with  $I_{\text{RMP}} = 3.5$  kA. The divertor heat flux profile is split and has a toroidally asymmetric structure with RMPs. Furthermore, the heat flux

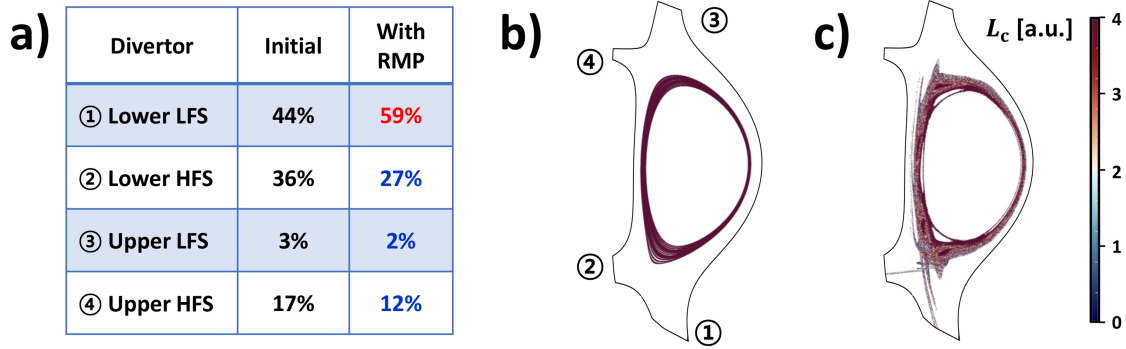


FIG. 14. a) Comparison of the ratio of integrated heat fluxes on four divertor plates before and after RMP application. Each divertor plate is marked on the poloidal cross-section, which shows the Poincaré plots in RZ-space for the cases b) without and c) with RMPs. The color contours describe the connection length  $L_c$ .

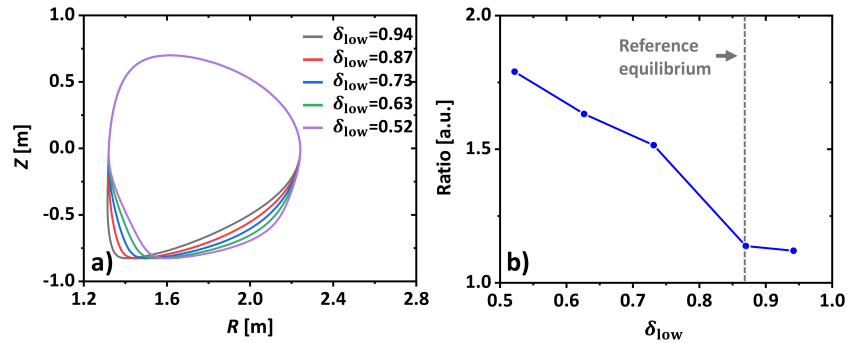


FIG. 15. a) Comparison of the plasma boundaries for the lower triangularity,  $\delta_{10w}$ , scan. The calculated ratio of  $\xi_\psi$  at HFS and LFS is shown in b). The  $\delta_{10w}$  value of the reference equilibrium is marked as a dotted line in b).

amplitude increases after RMP application. This becomes clear by comparing toroidally-averaged heat flux illustrated in Fig. 13(c). Here, the peak heat flux increases three times, showing good agreement with measured values using IR thermography [78]. Such an increase in divertor heat flux by RMPs is one of the distinguishing features in KSTAR [79] in that it is not common in other devices. Although heat flux splitting by RMPs is also observed [80, 81] in other devices, there is no significant change in the peak value.

It turns out that the increased heat flux on the lower divertor plate at LFS (LLFS) can be the result of heat redistribution on divertor plates. Figure 14(a) shows the normalized ratio of integrated heat fluxes on four divertor plates labeled in Fig. 14(b). It can be seen that the ratio on LLFS divertor increases with RMP while power deposition on other divertors decreases. If there

is no meaningful change in net power on divertors before and after RMP application, this change in the ratio will eventually increase the LLFS divertor heat flux, explaining why modeled peak heat flux increases at the LLFS divertor. Such a redistribution of powers on divertors stems from the tangled structure. Figure 12 shows that the tangle size and perturbation amplitude are stronger at the LFS than on the high-field side (HFS). These perturbations are directly linked to the divertor heat fluxes, leading to the increased flux on the LFS, resulting in an enhanced power ratio on the LLFS divertor. This is mainly due to enhanced conductive flux by the shorter connection length led by the tangles, as shown in Fig.14. Therefore, the poloidal asymmetric temperature perturbation (or tangle) can be the main reason for the change of the divertor heat flux observed both in experiment and simulation. Here, the size of the tangle is roughly proportional to the perturbed normal displacement ( $\xi_\psi$ ), and its poloidal asymmetry can be approximated to the ratio of  $\xi_\psi$  at LFS and HFS near the X-point,  $R_{HL} = \xi_{\psi,HFS} / \xi_{\psi,LFS}$ .

Previous work[82] shows that this ratio is sensitive to plasma shaping. In these simulations, the reference plasma has a large lower triangularity  $\delta_{low}=0.87$ , and strong asymmetry in tangles can be related to the shaping effect. To investigate this correlation,  $\delta_{low}$  is scanned from 0.5 to 0.9. The plasma parameters, including  $I_p$  and  $\beta$ , are fixed during the shaping scan. Because full calculation using JOREK is expensive for such a shaping scan, the IPEC code [83] is employed to capture the behavior of edge plasma response with different boundary shapes. Figure 15(a) presents the equilibria for the  $\delta_{low}$  scan and derived RMP response. As shown in Fig. 15(b),  $R_{HL}$  considerably decreases with  $\delta_{low}$ , supporting the above hypothesis. Therefore, an increasing peak heat flux on LLFS with RMPs may result from the strong shaping of the reference case. Because the fundamental goal of applying RMPs is to reduce the intensity of heat flux, these results emphasize the importance of considering the background heat flux in designing the ELM-free operation scenario using 3D fields.

We note that this modeling does not consider the exact divertor shape, the radiation, and accurate divertor transports. In addition, all simulated divertor heat flux profiles are scaled with  $\alpha$ ,

$$\alpha = \frac{P_H}{P_H - dW/dt}, \quad (3)$$

where  $P_H$  is an input heating power and  $W$  is the stored energy. When the RMP degrades the pedestal, this change propagates to the core region within hundreds of milliseconds. However, such a time scale is beyond the scope of this modeling, and  $dW/dt$  is not negligible in the whole

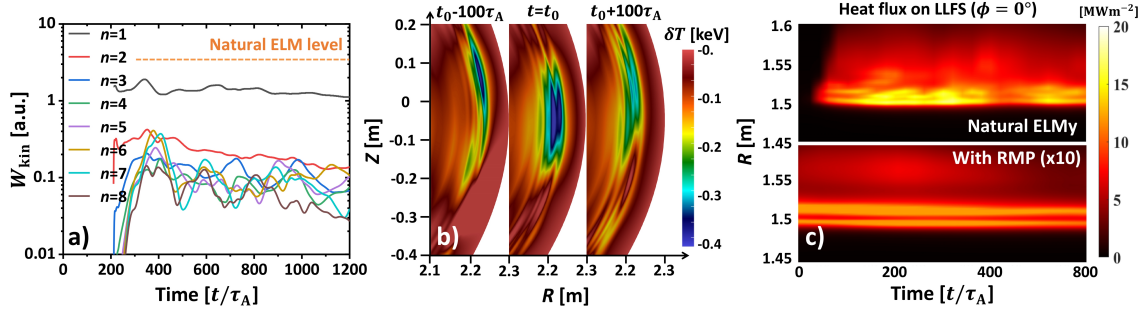


FIG. 16. a) Time evolution of the PBM harmonics of the kinetic energy for  $n=1-8$  with RMPs at  $I_{\text{RMP}}=3.5$  kA. The orange dotted line marks the maximum kinetic perturbation level in natural PBM simulations. b) Simulation results for the temperature fluctuation at three different time slices with  $\Delta t=200\tau_A$  with  $t_0=500\tau_A$ . c) The time traces of ELM heat flux profiles on the LLFS divertor at  $\phi = 0^\circ$  for the case without and with RMPs. The heat flux values with RMP are multiplied by 10 in c).

simulation, even if the pedestal profile is saturated in time. For this reason,  $\alpha$  is applied to exclude the effect of  $dW/dt$  on the heat flux, and this scaled value may differ from the truly saturated values. Furthermore, the shaping scan results in Fig.15 can be less accurate as the IPEC code cannot treat the exact X-point geometry and resistive plasma response. These limitations in the modeling address the importance of a dedicated simulation study on the effect of RMPs on boundary regions. In addition, simultaneous measurement of divertor heat flux on LFS and HFS will be an effective dataset for future work.

#### IV. PBM SUPPRESSION BY RMP

To study the behavior of PBMs with RMPs, the same approach is used as done in Ref.[41], where  $n = 2-8$  harmonics are launched when the  $n=1$  RMP is fully established. In this way, the interaction between RMPs ( $n=1$ ) and PBMs ( $n > 1$ ) is evaluated self-consistently. Here,  $n > 8$  modes are also linearly unstable. However,  $n > 8$  modes are excluded to meet the limitation of computing resources and as the lower  $n$  modes are more dominant during the non-linear phase. The simulation result for the case with experimentally relevant  $I_{\text{RMP}} = 3.5$  kA is presented in Fig. 16(a). The orange dotted line indicates the maximum value of perturbed kinetic energy in the natural PBM simulation. In the simulation, only the  $n = 2$  mode shows a tiny burst in the initial phase, and all modes become saturated [41, 43, 45], showing small oscillations. Interestingly, the PBM structures remain in the mode suppression phase, as shown in Fig. 16(b), indicating that

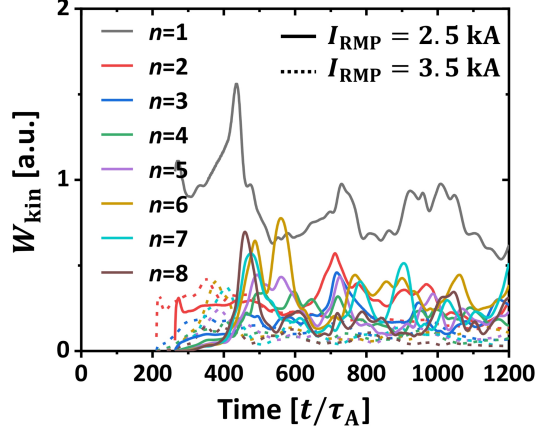


FIG. 17. Comparison of PBM harmonics of the kinetic energy for  $n=1-8$  with  $I_{RMP}=2.5$  (solid) and 3.5 kA (dotted lines). The pedestal profiles are similarly matched in these cases before including  $n > 1$  harmonics.

PBMs under RMPs are nonlinearly saturated at a low level (or suppressed without a crash) rather than linearly stabilized. This may explain why edge filament structures are observed during the ELM suppression experiment. In addition, the filament structures are spatially locked during the suppression phase in the simulation, as observed in previous work [43, 45]. As shown in Fig. 16(b), the mode structure exhibits only oscillatory movements within  $200\tau_A$ , which agrees well with the experimental trend [40, 84]. We note that the filaments have a weak coherent structure because of the spatial overlap of saturated multiple harmonics with similar amplitudes.

The ELMy heat flux with RMPs is also investigated. Figure 16(c) shows the time traces of heat flux on the LLFS divertor ( $\phi = 0^\circ$ ) for the case without and with RMPs. For the natural PBM case, the instantaneous peak heat flux exceeds  $20 \text{ MW/m}^2$ . On the other hand, its peak value remains lower than  $1.5 \text{ MW/m}^2$  with RMPs. Here, the peak heat flux with RMPs does not considerably deviate from the background values. Therefore, suppression of PBMs significantly reduces the ELM heat flux, which is consistent with the experimental trend. We note that the comparison between the simulation and the experiment here is limited to the general qualitative behavior rather than quantitative details. In future work, a dedicated dataset including measured edge fluctuations will be essential to validate the modeling results and improve the analysis of PBM suppression dynamics.

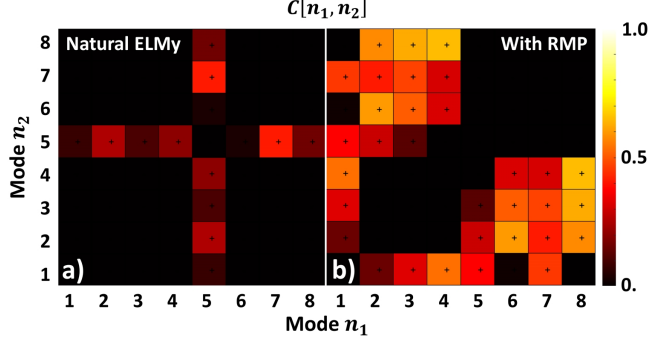


FIG. 18. Comparison of the time correlation coefficient for  $W_{\text{kin}}$  among the  $n=1-8$  harmonics for the a) natural ELMy and b) PBM suppression cases shown in Fig. 16. A larger value means a higher correlation between mode components.

## V. NONLINEAR INTERACTION BETWEEN RMP AND PBM

As widely accepted, a degraded mean pedestal pressure may be the reason for suppressed PBMs. Additionally, previous studies [41, 43–45] suggested that PBM suppression can also be related to the mode interaction of PBMs ( $n > 1$ ) with RMP response ( $n=1$ ). To find the contributors to PBM suppression, the nonlinear mode evolution is checked with the degraded mean pedestal profile of  $I_{\text{RMP}} = 3.5$  kA. It is not shown here, but PBMs are linearly stable with a reduced pedestal profile. However, when  $I_{\text{RMP}}$  of 2.5 kA is applied, as shown in Fig. 17, PBMs are non-linearly unstable even with the substantially degraded pedestal. The fact that the reduced RMP strength results in unstable PBMs even if the pedestal profile remains degraded, suggests that the RMP-PBM interactions can directly contribute to PBM suppression.

Detailed analysis of the RMP-PBM interaction reveals that it can contribute to PBM suppression by enhancing the interactions between PBMs. The mode interactions between RMPs ( $n=1$ ) and PBMs can be quantified as  $C[n_1, n_2]$ , the time correlation coefficient for  $n_1$  and  $n_2$  harmonics mode amplitude ( $W_{\text{kin}}$ ).  $C[n_1, n_2]$  is calculated during the nonlinear phase, where the mode crash occurs. The result is presented in Fig. 18. In the natural ELMy case, the interactions between harmonics are mainly done by  $n=5$ , which is the most unstable mode. However, in the PBM suppression case, the mode interactions appear over a wide range of  $n$ . This result addresses that RMPs enhance energy exchanges between PBMs. When the energy transfer between modes increases (or nonlinear damping), a single PBM cannot grow enough to cause a crash because it loses energy to other modes. Therefore, RMPs mediate the interaction between PBM harmonics

and result in states with saturated or suppressed modes. This result shares a similar idea with the previous study [85] that the large mode crash disappears with increased mode interactions. Therefore, PBM suppression can be achieved due to decreased linear driving and nonlinear damping of PBMs by RMP-induced pedestal transport and mode interaction.

In order to clarify how the mode interaction occurs in time and space, the mode interactions are quantified in the PBM suppressed case by defining  $\Gamma_n$  as

$$\Gamma_n = j_{\phi,n}[\psi_{n'}, u_{n-n'}]^*, \quad (4)$$

where  $n$  and  $n'$  are the toroidal mode numbers,  $j_{\phi}$  is the toroidal current density,  $u_{n-n'}$  is the electrostatic potential of toroidal mode  $(n-n')$ , and  $[..]^*$  is a conjugate of Poisson bracket.  $\Gamma_n$  describes the nonlinear magnetic energy transfer of mode  $n$  via the Ohmic dissipation, which represents an exchange between the magnetic field energy and the kinetic energy. A previous study [44] shows that this quantity effectively measures nonlinear energy exchanges between harmonics. Here,  $\Gamma_n$  is calculated at the LFS mid-plane of the  $q = 5$  surface ( $\psi_N = 0.94$ ) to quantify the nonlinear mode interactions. Time slice  $t=500\tau_A$  of Fig. 16 is selected for the calculation. Figure 19(a) shows the result of  $\Gamma_n$  with different  $n$ 's. It clearly shows that mode interactions are led by the  $n=1$  component, which means that the RMP-induced magnetic perturbations play a major role. On the other hand, the electrostatic potential does not play a considerable role as the interactions among  $n - n' = 1$  are negligible. Therefore, it can be confirmed that the RMP field penetration and sufficient perturbed field by RMP ( $n'=1$ ),  $\psi_{\text{RMP}}$ , are vital for the RMP-PBM interaction and ELM suppression.

The perturbed field  $\psi_{\text{RMP}}$  includes both resonant and non-resonant components, where the first one is driven by tearing, and the other comes from the KPM response. To investigate the role of each component,  $\Gamma_n$  is calculated again with  $n=1$  but with separating poloidal mode number  $m$  of  $\psi_{\text{RMP},m}$  ( $n'=1, \text{RMP}$ ) at the same location on the  $q = 5$  surface, where  $\psi_{\text{RMP}} = \sum_m \psi_{n'=1,m}$ . In this way, we can define  $\Gamma_n(m)$  as  $j_{\phi,n}[\psi_{n',m}, u_{n-n'}]^*$ . As shown in Fig. 19(b), the interactions mainly occur by  $m=5$  and its side-bands, which are the resonant components. It indicates that the tearing components are the main contributor and emphasizes the importance of sufficient islands for RMP-PBM interaction. In addition,  $\Gamma_n$  for multiple radial points on the LFS mid-plane is derived and illustrated in Fig. 19(c). It shows that the energy interactions of lower- $n$  harmonics occur in a wide radial range. However,  $\Gamma_n$  of higher- $n$  modes is localized to the  $q = 5$  surface near the pedestal top. Because the interactions between PBMs should occur for all  $ns$  for complete mode suppression,

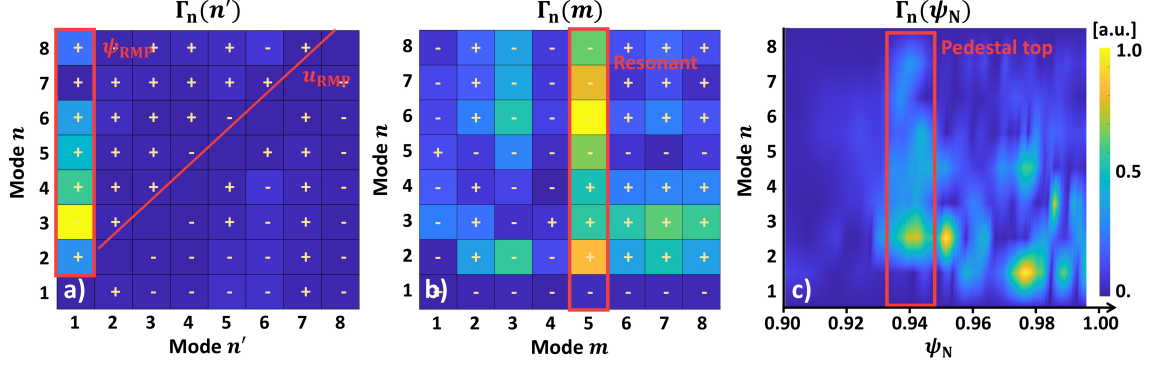


FIG. 19. a)  $\Gamma_n$  vs mode  $n$  and  $n'$  at the  $q=5$  surface. The values which are correlated with  $\psi_{\text{RMP}}$  and  $u_{\text{RMP}}$  are marked as the red box and line, respectively. b)  $\Gamma_n$  vs toroidal ( $n$ ) and poloidal ( $m$ ) mode numbers with  $n'=1$  at the  $q=5$  surface. The resonant component are marked as a red box. c)  $\Gamma_n$  vs mode  $n$  and  $\psi_N$ . The pedestal top region is presented as a red box. Here, the sign of values is also shown as ‘ $\pm$ ’ marks.

this trend addresses the importance of sufficient tearing components at the inner pedestal region. Here, the reason why  $\Gamma_n$  of higher- $n$  mainly occurs at the rational surface near the pedestal top is not yet clear, but this may be related to the PBM characteristics. As the  $n$  of PBMs increases, the ballooning component grows over the peeling component. Then, the normalized mode amplitude near the top of the pedestal increases while the very edge amplitude decreases. The comparison of radial  $\delta j_\phi$  structure for  $n = 4$  and  $8$  in Fig. 20 clearly shows this. As a result,  $\Gamma_n$  near the pedestal top also increases with  $\delta j_{\phi,n}$  and may become dominant. Interestingly, recent numerical studies [63, 86] revealed a strong correlation between PBM suppression and island formation at the pedestal top. The island can strengthen the RMP-PBM interaction and lead to the PBM suppression, this nonlinear analysis is consistent with the previous finding.

Based on these findings, ELM suppression requires consistent energy exchange between PBMs and RMPs. Therefore, their relative phasing or spatial overlap may have to be well-maintained in time for sufficient mode interactions. Since the RMP response ( $n=1$ ) is not rotating, such mode overlap depends on the perpendicular rotation ( $V_{\text{PBM}}$ ) of the PBM structure. Therefore, to keep the phasing constant,  $V_{\text{PBM}}$  needs to be small. Although its mechanism is unknown yet, the spatially locked PBM structure in the RMP-PBM simulation is also consistent with this concept. In addition, the previous studies reported that  $V_{\text{PBM}}$  could be increased with  $E \times B$  rotation ( $V_E$ ) near the pedestal region [45, 49, 87]. Therefore, small  $V_E$  may be favorable, which enhances the mode interaction. It might also be related to the role of  $V_E \approx 0$  [18, 38, 88] near the pedestal for PBM

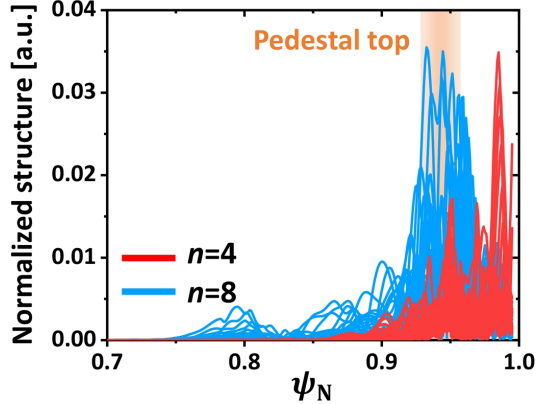


FIG. 20. Radial structure of the  $n=4$  (red) and 8 (blue) harmonics in the PBM-suppression case. The pedestal top region is colored orange.

suppression.

## VI. CONCLUSION

The mechanism of  $n=1$  RMP-driven pedestal transport and suppression of PBMs in KSTAR has been studied using coupled PENTRC and JOREK simulations in order to include the effect of NTV fluxes. KPM, tearing response, NTV transport, and mode interactions have been investigated. In response to applied RMPs, the plasma deformation and islands occurred at the pedestal. In addition, the plasma deformation drives NTV fluxes. These responses increase the radial transport in the pedestal and result in a fair agreement between the modeling and the experimentally observed density pump-out. The ITER 3D coil systems will be capable of inducing relatively large  $\delta B/B$  perturbations in the plasma edge[89]. A combination of the  $\sim (\delta B/B)^2$  scaling and kinetic resonances in the low collisionality, low Er regime of the ITER edge leads to the expectation of significant neoclassical fluxes in the plasma edge when utilizing these ITER 3D coils[90]. This work thus motivates a need for full JOREK simulations of the ITER edge response with coupled neoclassical effects to predict the impact RMPs onto the expected pedestal density in ITER.

However, these results still have limitations in the model, and they may be insufficient to fully explain the RMP-induced pedestal transport. This suggests that further physics, such as polarization drift and turbulence, must also be included to explain the pedestal degradation. The effect of RMPs on divertor heat flux is also investigated. Modeling shows that the heat flux on the lower LFS divertor can be significantly increased with RMPs due to poloidal asymmetric tangle struc-

tures and heat redistribution among the divertor plates. Although RMPs are still highly advantageous to the divertor since the ELMs themselves are suppressed, the localization of the inter-ELM heat-flux on a single divertor is unfavorable to the plasma-facing components, and must be taken into account when optimizing a long pulse ELM-free scenario.

The modeling of PBMs with RMPs showed that the PBMs are suppressed for experimental RMP coil current of  $I_{\text{RMP}} = 3.5$  kA. Locking of PBMs is observed during the mode suppression, which agrees well with the experiment. Nonlinear analysis shows that PBM suppression is attributable to the degraded pedestal and direct interaction between PBMs and RMPs. This interaction can increase the spectral transfer between PBM harmonics, preventing significant growth and the crash of unstable modes. It leads to the saturation of modes rather than bursty mode behavior. A resonant perturbed magnetic field mediates the mode interaction, and the tearing component near the pedestal top is vital in enhancing the mode interaction between higher- $n$  PBMs. This is consistent with previous findings [86] where the magnetic island at the top of the pedestal plays a critical role in accessing PBM suppression. This work suggests that small  $V_{\text{PBM}}$  at the pedestal is advantageous to PBM suppression as the relative phasing between PBMs and RMP remains constant, leveraging the energy exchange between RMP and PBMs. Lastly, it is noteworthy to summarize the assumptions used in this work. They are 1) 30x elevated resistivity, 2) assumption of same ion and electron temperature, 3) exclusion of higher ( $n > 8$ ) harmonics even though they are linearly unstable, 4) considerable uncertainty in measured pedestal profile, 5) assumption of uniform temperature along field lines and approximated displacement, 6) neglect of long-term change in background source and anomalous transport, and 7) of the non-linear effect of NTV on the plasma rotation. This will lead to some limitations in accurately describing the island formation, edge transport, NTV, and RMP-induced mode couplings. Because these components are critical in understanding 3D physics, further work will be needed that successively drops these assumptions and includes more advanced physics to improve the predictive capability for future devices.

## ACKNOWLEDGMENTS

The authors would like to express their deepest gratitude to KSTAR team for the extensive supports on the RMP-ELM suppression experiment. This material was supported by the U.S. Department of Energy, under Awards DE-SC0020372 & DE-AC52-07NA27344. This research

was also supported by R&D Program of "KSTAR Experimental Collaboration and Fusion Plasma Research(EN2021-12)" through the Korea Institute of Fusion Energy(KFE) funded by the Government funds. Computing resources were provided on the KFE computer, KAIROS, funded by the Ministry of Science and ICT of the Republic of Korea (KFE-EN2241-8). Part of this work has been carried out within the framework of the EUROfusion Consortium and has received funding from the Euratom research and training program 2014-2018 and 2019-2020 under grant agreement No 633053. The views and opinions expressed herein do not necessarily reflect those of the European Commission.

---

- [1] F. Wagner *et al.* *Physical Review Letters* **53**, 15, 1453 (1984).
- [2] C. Challis *et al.* *Nuclear Fusion* **55**, 5, 053031 (2015).
- [3] R. J. Bickerton *et al.* *Nature Physical Science* **229**, 4, 110 (1971).
- [4] H. Zohm *et al.* *Nuclear Fusion* **32**, 3, 489 (1992).
- [5] J. W. Connor *et al.* *Physics of Plasmas* **5**, 7, 2687 (1998).
- [6] G. Huysmans *et al.* *Nuclear Fusion* **47**, 7, 659 (2007).
- [7] A. Loarte *et al.* *Nuclear Fusion* **54**, 3, 033007 (2014).
- [8] J. Gunn *et al.* *Nuclear Fusion* **57**, 4, 046025 (2017).
- [9] T. Hirai *et al.* *Nuclear Materials and Energy* **9**, 616 (2016).
- [10] T. E. Evans *et al.* *Physical Review Letters* **92**, 23 (2004).
- [11] T. E. Evans *et al.* *Nature Physics* **2**, 6, 419 (2006).
- [12] T. Evans *et al.* *Nuclear Fusion* **48**, 2, 024002 (2008).
- [13] O. Schmitz *et al.* *Physical Review Letters* **103**, 16, 165005 (2009).
- [14] Y. M. Jeon *et al.* *Physical Review Letters* **109**, 3 (2012).
- [15] R. Nazikian *et al.* *Physical Review Letters* **114**, 10, 105002 (2015).
- [16] C. Paz-Soldan *et al.* *Physical Review Letters* **114**, 10, 105001 (2015).
- [17] Y. Sun *et al.* *Physical Review Letters* **117**, 11 (2016).
- [18] W. Suttrop *et al.* *Plasma Physics and Controlled Fusion* **59**, 1, 014049 (2016).
- [19] P. B. Snyder *et al.* *Physics of Plasmas* **19**, 5, 056115 (2012).
- [20] T. Evans *et al.* *Nuclear Fusion* **45**, 7, 595 (2005).
- [21] R. A. Moyer *et al.* *Physics of Plasmas* **12**, 5, 056119 (2005).

- [22] M. E. Fenstermacher *et al.* *Physics of Plasmas* **15**, 5, 056122 (2008).
- [23] F. Orain *et al.* *Nuclear Fusion* **57**, 2, 022013 (2017).
- [24] Q. M. Hu *et al.* *Physics of Plasmas* **26**, 12, 120702 (2019).
- [25] R. Fitzpatrick *et al.* *Physics of Plasmas* **28**, 8, 082511 (2021).
- [26] S. Mordijck *et al.* *Physics of Plasmas* **19**, 2, 024504 (2012).
- [27] G. McKee *et al.* *Nuclear Fusion* **53**, 11, 113011 (2013).
- [28] S. Mordijck *et al.* *Nuclear Fusion* **54**, 8, 082003 (2014).
- [29] C. Sung *et al.* *Physics of Plasmas* **24**, 11, 112305 (2017).
- [30] T. M. Bird *et al.* *Nuclear Fusion* **53**, 1, 013004 (2013).
- [31] I. Holod *et al.* *Nuclear Fusion* **57**, 1, 016005 (2017).
- [32] G. J. Choi *et al.* *Nuclear Fusion* **58**, 2, 026001 (2017).
- [33] R. Wilcox *et al.* *Nuclear Fusion* **57**, 11, 116003 (2017).
- [34] S. Taimourzadeh *et al.* *Nuclear Fusion* **59**, 4, 046005 (2019).
- [35] R. Hager *et al.* *Nuclear Fusion* **59**, 12, 126009 (2019).
- [36] N. M. Ferraro. *Physics of Plasmas* **19**, 5, 056105 (2012).
- [37] M. Becoulet *et al.* *Nuclear Fusion* **52**, 5, 054003 (2012).
- [38] R. Fitzpatrick. *Physics of Plasmas* **27**, 4, 042506 (2020).
- [39] Y. Liu *et al.* *Nuclear Fusion* **60**, 3, 036018 (2020).
- [40] J. Lee *et al.* *Physical Review Letters* **117**, 7 (2016).
- [41] M. Bécoulet *et al.* *Physical Review Letters* **113**, 11, 115001 (2014).
- [42] D. Chandra *et al.* *Nuclear Fusion* **57**, 7, 076001 (2017).
- [43] F. Orain *et al.* *Physics of Plasmas* **26**, 4, 042503 (2019).
- [44] S. Kim *et al.* *Current Applied Physics* **19**, 3, 266 (2019).
- [45] S. Kim *et al.* *Nuclear Fusion* **60**, 2, 026009 (2020).
- [46] G. T. A. Huysmans *et al.* *Plasma Physics and Controlled Fusion* **51**, 12, 124012 (2009).
- [47] M. Hoelzl *et al.* *Nuclear Fusion* **61**, 6, 065001 (2021).
- [48] N. C. Logan *et al.* *Physics of Plasmas* **20**, 12, 122507 (2013).
- [49] M. Bécoulet *et al.* *Nuclear Fusion* **57**, 11, 116059 (2017).
- [50] G. V. Pereverzev *et al.* *ASTRA user guide IPP-Report IPP 5/98* page 147 (2002).
- [51] N. Ferraro *et al.* *Nuclear Fusion* **53**, 7, 073042 (2013).
- [52] F. Orain *et al.* *Physics of Plasmas* **20**, 10, 102510 (2013).

- [53] J. R. Cary *et al.* *Physics of Plasmas* **4**, 9, 3323 (1997).
- [54] J.-k. Park *et al.* *Physical Review Letters* **102**, 6, 065002 (2009).
- [55] P. B. Snyder *et al.* *Physics of Plasmas* **16**, 5, 056118 (2009).
- [56] L. Lao *et al.* *Nuclear Fusion* **25**, 11, 1611 (1985).
- [57] W.-H. Ko *et al.* *Review of Scientific Instruments* **81**, 10, 10D740 (2010).
- [58] J. H. Lee *et al.* *Review of Scientific Instruments* **81**, 10, 10D528 (2010).
- [59] M. Kim *et al.* *Nuclear Fusion* **54**, 9, 093004 (2014).
- [60] G. S. Yun *et al.* *Review of Scientific Instruments* **81**, 10, 10D930 (2010).
- [61] G. S. Yun *et al.* *Review of Scientific Instruments* **85**, 11, 11D820 (2014).
- [62] A. B. Mikhailovskii. *Plasma Physics and Controlled Fusion* **40**, 11, 1907 (1998).
- [63] Q. Hu *et al.* *Nuclear Fusion* **60**, 7, 076001 (2020).
- [64] Q. Hu *et al.* *Physical Review Letters* **125**, 4, 045001 (2020).
- [65] I. Krebs *et al.* *Physics of Plasmas* **20**, 8, 082506 (2013).
- [66] M. Kim *et al.* *Physics of Plasmas* **26**, 5, 052502 (2019).
- [67] S. Pamela *et al.* *Plasma Physics and Controlled Fusion* **58**, 1, 014026 (2016).
- [68] J. G. Bak *et al.* *Review of Scientific Instruments* **82**, 6, 063504 (2011).
- [69] M. Bécoulet *et al.* *Nuclear Fusion* **48**, 2, 024003 (2008).
- [70] Y. Liu *et al.* *Plasma Physics and Controlled Fusion* **58**, 11, 114005 (2016).
- [71] D. Reiser *et al.* *Physics of Plasmas* **16**, 4, 042317 (2009).
- [72] K. C. Shaing. *Physics of Fluids* **26**, 11, 3315 (1983).
- [73] Y. Liu *et al.* *Nuclear Fusion* **51**, 8, 083002 (2011).
- [74] F. Waelbroeck *et al.* *Nuclear Fusion* **52**, 7, 074004 (2012).
- [75] J. D. Callen *et al.* *Nuclear Fusion* **53**, 11, 113015 (2013).
- [76] Q. Yu *et al.* *Nuclear Fusion* **51**, 7, 073030 (2011).
- [77] R. Hager *et al.* *Physics of Plasmas* **27**, 6, 062301 (2020).
- [78] H. Lee *et al.* *Nuclear Materials and Energy* **12**, 541 (2017).
- [79] Y. In *et al.* *Nuclear Fusion* **57**, 11, 116054 (2017).
- [80] M. Jakubowski *et al.* *Nuclear Fusion* **49**, 9, 095013 (2009).
- [81] A. Thornton *et al.* *Journal of Nuclear Materials* **438**, S199 (2013).
- [82] L. Li *et al.* *Nuclear Fusion* **56**, 12, 126007 (2016).
- [83] J.-k. Park *et al.* *Physics of Plasmas* **14**, 5, 052110 (2007).

- [84] J. Lee *et al.* *Nuclear Fusion* **59**, 6, 066033 (2019).
- [85] P. Xi *et al.* *Physical Review Letters* **112**, 8, 085001 (2014).
- [86] Q. M. Hu *et al.* *Physics of Plasmas* **28**, 5, 052505 (2021).
- [87] J. A. Morales *et al.* *Physics of Plasmas* **23**, 4, 042513 (2016).
- [88] C. Paz-Soldan *et al.* *Nuclear Fusion* **59**, 5, 056012 (2019).
- [89] Q. Hu *et al.* *Nuclear Fusion* **61**, 10, 106006 (2021).
- [90] Y. Liu *et al.* *Nuclear Fusion* **55**, 6, 063027 (2015).